Available online at www.sciencedirect.com

SciVerse ScienceDirect

Geochimica et Cosmochimica Acta 86 (2012) 37–51

Geochimica et Cosmochimica Acta

www.elsevier.com/locate/gca

Internal ^{26}Al–^{26}Mg isotope systematics of a Type B CAI: Remelting of refractory precursor solids

Noriko T. Kita [a,*], Takayuki Ushikubo [a], Kim B. Knight [b,c,1], Ruslan A. Mendybaev [b,c], Andrew M. Davis [b,c,d], Frank M. Richter [b,c], John H. Fournelle [a]

[a] WiscSIMS, Department of Geoscience, University of Wisconsin-Madison, 1215 W. Dayton St., Madison WI 53706, United States
[b] Chicago Center for Cosmochemistry, The University of Chicago, Chicago, IL 60637, United States
[c] Department of the Geophysical Sciences, The University of Chicago, Chicago, IL 60637, United States
[d] Enrico Fermi Institute, The University of Chicago, Chicago, IL 60637, United States

Received 2 May 2011; accepted in revised form 10 February 2012; available online 1 March 2012

Abstract

High precision SIMS ^{26}Al–^{26}Mg isotope analyses were performed for a pristine Type B1 CAI Leoville 3535-1 on multiple mineral phases that include aluminum-rich zoned melilite mantle ($Åk_{20}$–$Åk_{60}$), magnesium-rich melilite ($Åk_{70}$), fassaite, spinel and anorthite in the core. The data yield a well-defined internal isochron with an inferred initial $^{26}Al/^{27}Al$ ratio of $(5.002 \pm 0.065) \times 10^{-5}$, which is lower than those of bulk CAIs and pristine fine-grained CAIs. Assuming homogeneous distribution of ^{26}Al in the early solar system, Leoville 3535-1 formed ~50 ka after the time corresponding to the bulk CAI isochron. One anorthite analysis near the grain boundary adjacent to melilite shows sub-μm-scale heterogeneous magnesium distribution, though the ^{26}Al–^{26}Mg data plot on the isochron regression. Thus, the internal ^{26}Al–^{26}Mg system of the CAI remained closed since the last melting event that crystallized anorthite.

High precision magnesium isotope analyses of magnesium-rich minerals (fassaite, magnesium-rich melilite, and spinel) show a small amount of scatter from the regression line (~0.1‰) beyond analytical uncertainties. Most spinel and some fassaite data are systematically displaced below and above the regression line, respectively. It is likely that spinel remained unmelted at the time of the last melting event, while fassaite and anorthite crystallized from a partial melt. The regression line made by fassaite and anorthite data shows an initial $^{26}Al/^{27}Al$ ratio indistinguishable from that using all data. Mass dependent fractionation of magnesium isotopes in spinel is the same as those in melilite and fassaite ($\delta^{25}Mg \sim 5‰$), indicating that magnesium isotope fractionation, presumably from evaporative magnesium loss, predated the last melting event. Thus a majority of the CAI appears to have escaped magnesium isotope exchange with nebular gas during the last melting event, except for the outer rim of the melilite mantle that shows slightly lower $\delta^{25}Mg$ values.

The ^{26}Al–^{26}Mg systematics of this Leoville Type B CAI suggest it experienced a final melting event at ~50 ka after the initial Al–Mg fractionation event. This may correspond to melting during the active protostar stage (known as "Class I"), during which sporadic high temperature heating events repeatedly affected refractory solids in the solar nebula.

* Corresponding author.
E-mail address: noriko@geology.wisc.edu (N.T. Kita).
[1] Present address: Lawrence Livermore National Laboratory, Livermore, CA 94550, United States.

0016-7037/$ - see front matter © 2012 Elsevier Ltd. All rights reserved.
http://dx.doi.org/10.1016/j.gca.2012.02.015

1. INTRODUCTION

Calcium-, aluminum-rich inclusions (CAIs) in primitive meteorites (e.g., MacPherson et al., 2005; MacPherson, 2007) are the oldest solar system objects measured by the Pb–Pb absolute chronometer (Amelin et al., 2002, 2010; Connelly et al., 2008; Bouvier and Wadhwa, 2010). Unaltered phases in these objects have large ^{16}O enrichments relative to Earth, the Moon and most bulk meteorites ($\delta^{18}O \sim \delta^{17}O \sim -50‰$; Clayton et al., 1973), an isotopic composition similar to that of the Sun recently estimated from the analysis of solar wind collected by the Genesis space craft (McKeegan et al., 2011). CAIs occur in almost all types of chondritic meteorites and also among particles collected by the Stardust mission from comet 81P/Wild 2 (McKeegan et al., 2006; Zolensky et al., 2006; Simon et al., 2008), indicating that CAIs are ubiquitously distributed throughout the early solar system. Shu et al. (1996) suggested that CAIs formed close to the young sun, and were then lifted and transported to the asteroidal belt by a magnetically driven wind (X-wind model). Cuzzi et al. (2003) suggested CAIs were originally formed in hot inner solar nebula and transported to asteroid regions by outward radial diffusion in a weakly turbulent disk. Ciesla (2007) further showed high efficiency of outward radial transport by a two dimensional model that explains existence of CAIs as far as comet-forming regions.

Lee et al. (1977) reported the first clear evidence of in-situ decay of ^{26}Al (half life; ~0.7 Ma) from the mineral separates of the Allende CAI "WA", showing the correlated excess of ^{26}Mg from the decay of ^{26}Al with $^{27}Al/^{24}Mg$ ratios and inferred initial $^{26}Al/^{27}Al$ ratios of $(5.1 \pm 0.6) \times 10^{-5}$. MacPherson et al. (1995) summarized the literature data and showed that most CAIs consistently have an initial $^{26}Al/^{27}Al$ ratio of $\sim 5 \times 10^{-5}$, which is referred to as the "canonical" value. Exceptions are those called FUN (fractionation and unidentified nuclear effects, e.g., Wasserburg et al., 1977) CAIs and hibonite-bearing CAIs (Fahey et al., 1987; Ireland, 1988) with low inferred initial $^{26}Al/^{27}Al$ ratios ($\leqslant 10^{-6}$), which might indicate minor heterogeneity of ^{26}Al in the early solar nebula (MacPherson et al., 1995). For normal CAIs, it was not clear that there was any significant spread of initial $^{26}Al/^{27}Al$ ratios among CAIs, because of limited analytical precision and possible later disturbance of some of the CAIs (e.g., Podosek et al., 1991; LaTourrette and Hutcheon, 1999).

Recently, several studies have measured the initial $^{26}Al/^{27}Al$ ratios of CAIs with significantly improved analytical precision using multicollector inductively coupled plasma mass spectrometers (MC-ICPMS) or multicollector secondary ion mass spectrometers (MC-SIMS). There has been a vigorous debate as to the actual value of initial $^{26}Al/^{27}Al$ ratio of CAIs, with values as high as $(6–7) \times 10^{-5}$ being proposed (Bizzarro et al., 2004, 2005; Young et al., 2005; Thrane et al., 2006; Cosarinsky et al., 2007; Baker, 2008; Jacobsen et al., 2008; MacPherson et al., 2010). Recent estimates of the initial $^{26}Al/^{27}Al$ ratios of bulk CAIs in CV3 chondrites from two different laboratories show consistent values of $(5.23 \pm 0.13) \times 10^{-5}$ (Jacobsen et al., 2008) and $(5.25 \pm 0.02) \times 10^{-5}$ (Larsen et al., 2011) based on the well-defined isochron regressions. Several data from in-situ techniques such as laser ablation (LA) MC-ICPMS and MC-SIMS suggested the elevated initial $^{26}Al/^{27}Al$ ratios (e.g., Taylor et al., 2005; Young et al., 2005; Cosarinsky et al., 2007; Connolly et al., 2009, 2010; Simon and Young, 2011), though some of these data are scattered in the ^{26}Al–^{26}Mg isochron diagrams. It should be mentioned that many CAIs might have experienced alteration in their parent bodies, such as thermal metamorphism, aqueous alteration and shock reheating that can partially reset inferred $^{26}Al/^{27}Al$ ratios (e.g., Podosek et al., 1991; Nakamura et al., 1992; Caillet et al., 1993; Fagan et al., 2007). Formation of secondary minerals in the CAIs might cause either open or closed system redistribution of aluminum and magnesium, which may explain the disturbed data on the Al–Mg isochron diagram. In such cases, accurate and reliable initial $^{26}Al/^{27}Al$ ratios would not be obtained.

Here, we report a high precision MC-SIMS Al–Mg isotope study of a pristine large igneous Type B1 CAI (Leoville 3535-1). This CAI has no petrologic signs of secondary mineralization. The improved analytical precision of the latest generation of SIMS (CAMECA IMS-1280 at the University of Wisconsin-Madison; WiscSIMS, Valley and Kita, 2009; Kita et al., 2009a) allows us to evaluate the linearity of data in an isochron diagram and to test whether the Al–Mg isotope system in this CAI remained closed.

2. ANALYTICAL METHODS

2.1. Sample

The sample used in the present study is a large (8×6 mm) Type B1 CAI (USNM 3535-1) from the Leoville CV3 chondrite (Fig. 1). The CAI was originally chosen for a study of the internal distribution of magnesium and silicon isotope fractionations (Richter et al., 2007b; Knight et al., 2009). The outer edge of the CAI is surrounded by a thick (500 μm) melilite mantle that shows major element zoning with increasing åkermanite (Åk) contents from the rim to the interior ($Åk_{20–60}$). The texture and zoning indicate that the CAI crystallized inwards from the edge. Minor amounts of small spinel grains (<20 μm) also occur within mantle melilite. The core consists of åkermanite-rich melilite ($Åk_{65–80}$), fassaite, anorthite and spinel. TiO_2 contents of fassaite range from 2 to 10 wt.%, generally showing higher TiO_2 in fassaite within the melilite-rich mantle and lower TiO_2 in the core. There are no secondary minerals, such as nepheline and sodalite, observed in this CAI. SEM-EDX elemental maps of several areas of the CAI have been made and the Al–Mg chronology data reported in this paper are mainly from areas for which elemental maps are available.

The CAI section was originally potted in a 25 mm diameter, 13 mm thick phenolic mount. Because the sample degassed significantly and degraded the vacuum in the SIMS, which was problematic for silicon isotopic analyses and because the sample height was not compatible with the regular SIMS sample holder (12 mm), the sample was later made into a polished thin section with the original surface attached to a glass slide. The new thin section surface is within 40 μm of the original surface, but as the mirror

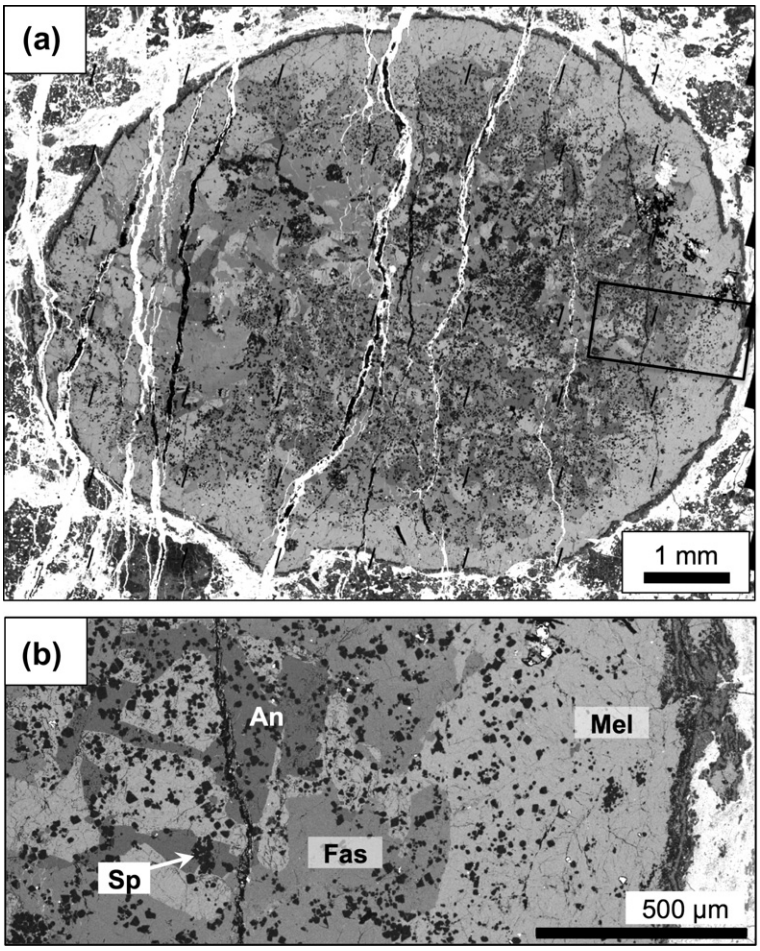

Fig. 1. Backscattered electron (BSE) images of the Leoville 3535-1 Type B1 CAI. (a) Image of whole CAI. The rectangle indicates the area shown as an expanded view in (b). (b) Expanded view of the CAI including the ~500 μm thick melilite (Mel) mantle. The core of the CAI consists of euhedral melilite (Mel), fassaite (Fas) and anorthite (An). Small grains of spinel (≤50 μm) are distributed throughout the inclusion.

image. The Al–Mg data reported in this paper were obtained from both the original mount and from the thin section.

2.2. Electron microscopy

In order to guide the location of the SIMS analyses, we obtained detailed secondary electron (SE) and backscattered electron (BSE) images using a JEOL JSM-5800LV scanning electron microscope (SEM) at the University of Chicago and a Hitachi S-3400 SEM at the University of Wisconsin-Madison. We also obtained elemental abundance maps of selected areas using an Oxford/Link ISIS-300 X-ray microanalysis system on the Chicago SEM. These maps were used to obtain maps of åkermanite content of melilite, which were very useful in selecting SIMS analysis points. Additional SE and BSE images were obtained after SIMS analyses, in order to examine the analyzed spots for potential inclusions and any other specific features that might have affected the SIMS analyses.

In the early stage of this work, we did not have multiple melilite standards with homogeneous aluminum and magnesium contents that could be used for SIMS $^{27}Al/^{24}Mg$ calibration. Therefore, the major element compositions of melilite in the CAI were obtained using the CAMECA SX-51 electron microprobe analyzer (EPMA) at the University of Wisconsin with an accelerating voltage of 15 kV and a focused beam of 12 nA. Pure synthetic åkermanite and gehlenite crystals (provided by M. Morioka of the Radioisotope Center at the University of Tokyo), which had been made as described in Morioka and Nagasawa (1991), were used as EPMA calibration standards. We also obtained major element compositions of fassaite at the location of the SIMS analyses using EPMA.

2.3. SIMS Al–Mg isotope analyses

The IMS-1280 at WiscSIMS was used for the SIMS Al–Mg isotope analyses. We used O^- primary ions with total impact energy of 23 kV (−13 kV at the ion source and +10 kV at the sample surface) and detected Mg^+ and Al^+ secondary ions. We applied two different analytical conditions using monocollection electron multiplier (mono-EM) and multicollection Faraday cups (MC-FC) for anorthite and other magnesium-rich minerals (melilite, fassaite, and spinel), respectively, due to the difference in secondary Mg^+ intensities. The CAI analyses were made in three

sessions; analyses of melilite mantle in MC-FC mode (S1), analyses of anorthite in mono-EM mode (S2), and analyses of three magnesium-rich minerals, melilite, fassaite, and spinel, in both mantle and core in MC-FC mode (S3).

2.3.1. Multicollection FC analysis

For multicollection FC analyses, the primary O^- ion beam was adjusted to produce a 20×25 μm oval shape with an intensity of 7 nA (spinel) and 20 nA (melilite and fassaite). By using the Duo lens (a new primary ion lens between the duoplasmatron ion source and primary beam mass filter), a primary ion intensity of 20 nA is easily obtained in Köhler illumination mode with mass and beam apertures of 200 and 750 μm diameter, respectively, where the mass aperture determines the size of the primary beam. In this condition, the SIMS analysis pits show a small amount of aberration and the carbon coat is removed over an area ~40 μm across, although the direct secondary ion images show that the majority of secondary ions are created only from a central 20×25 μm area. For spinel analyses with higher magnesium contents, we inserted a 400 μm beam aperture in order to remove the aberration of the primary beam. This condition made aiming of analysis location much easier for spinel with grain sizes typically smaller than 20 μm, although the primary beam intensity was reduced to 7 nA. Examples of SIMS pits produced by the different analysis conditions are shown in Fig. 2.

Secondary ion optics were adjusted to 200× magnification from the sample to the field aperture (6000 μm square) with mass resolving power of ~2500 (entrance slit; 90 μm and exit slit 500 μm). The contributions of $^{48}Ca^{++}$ and MgH^+ interferences to the Mg^+ mass spectrum were negligibly small. The energy slit was set to 40 eV. Four multicollection FC detectors were used to detect $^{24}Mg^+$, $^{25}Mg^+$, $^{26}Mg^+$ (with 10^{11} ohm resistors) and $^{27}Al^+$ (with 10^{10} ohm resistor) simultaneously, with $^{25}Mg^+$ set to the ion optical axis. Since the primary beam size transferred to the field aperture plane is comparable to the size of the field aperture, we applied XY-mode by using rectangular lenses at the coupling optics (between an electrostatic analyzer and a sector magnet) to produce a rectangular field aperture image with an aspect ratio of 5:1 at the entrance of the sector magnet, which reduced the aberration of the mass spectrum (De Chambost et al., 1997). In general, XY-mode would cause Y-deflection of the secondary beam but we did not find a significant difference in Y-deflection among four detectors. Secondary $^{24}Mg^+$ and $^{27}Al^+$ ions intensities were $(0.5–3) \times 10^8$ and $(1–4) \times 10^8$ cps (counts per second), respectively, depending on the mineral phase. A single analysis takes 8 min, including 60 s of presputtering, ~120 s for automated centering of the secondary optics, and 300 s of integration (10 s × 30 cycles) of the Mg^+ and Al^+ signals. The baseline of the FC detectors was monitored during presputtering and averaged over eight analyses. Due to difference in Mg^+ secondary intensities, we run each mineral separately. The melilite glass standard (~$Åk_{65}$), fassaite glass standard with 5 wt.% TiO_2 and natural spinel standard were repeatedly analyzed during melilite, fassaite and spinel analyses, respectively. In addition, multiple synthetic and natural standards were used to evaluate analytical conditions (Table EA1). A total of eight analyses of standard were obtained that bracket 8–10 unknown sample analyses. The

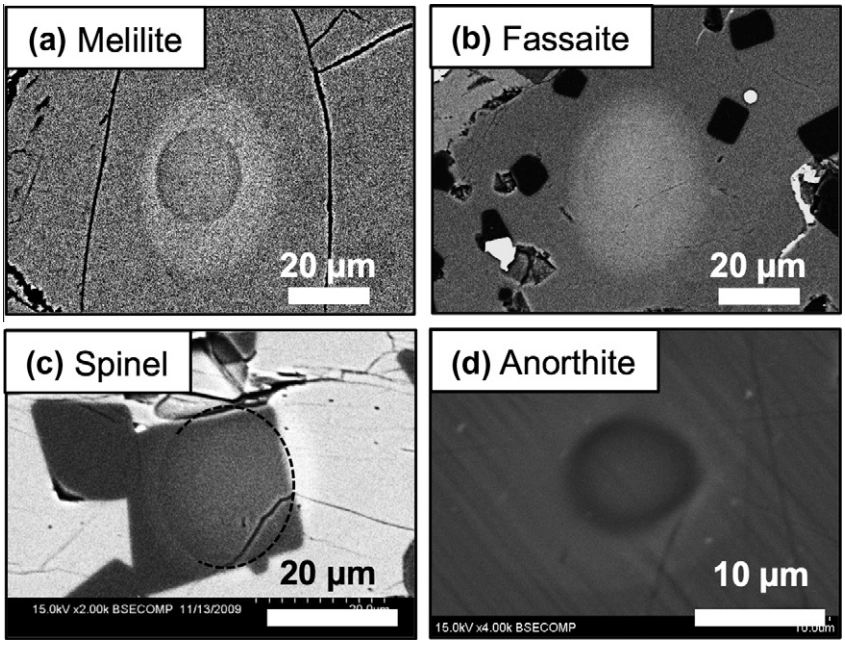

Fig. 2. Examples of SIMS spots in different minerals (shown as BSE images). (a) Melilite, (b) fassaite, (c) spinel, and (d) anorthite. Scale bars are 20 μm for (a–c) and 10 μm for (d). Melilite and fassaite analyses were made using 20 nA O^- primary ions, and the BSE shows a 25×20 μm oval beam spot with a surrounding area $\sim 40 \times 50$ μm where the surface carbon coating was removed. Spinel analyses were made using a 5–7 nA primary beam with ~25 μm well-defined flat-bottomed pits, although the edge of beam (partly shown as a dashed line) often overlaps with grain boundaries. Anorthite analyses were made using a 1 nA primary beam, resulting in ~8 μm flat-bottomed pits.

average values of the bracket standard analyses were used to correct for instrumental bias on the measured magnesium isotope ratios. The measured ratios ($^{25}Mg/^{24}Mg$ and $^{26}Mg/^{24}Mg$) are converted to δ notation ($\delta^{25}Mg$ and $\delta^{26}Mg$) by normalizing to the terrestrial reference ratios of $(^{25}Mg/^{24}Mg) = 0.12663$ and $(^{26}Mg/^{24}Mg) = 0.13932$ (Catanzaro et al., 1966), respectively.

The instrumental biases on $\delta^{25}Mg$ (mass-dependent fractionation) in melilite and fassaite were estimated from the analyses of multiple standards, which for melilite increases by 1‰ linearly from $Åk_{15}$ to $Åk_{100}$ and for fassaite decreases by 0.6‰ as TiO_2 increases from 2 to 10 wt.% (Tables EA2-1, EA2-2, and EA2-3). The $\delta^{25}Mg$ values in the CAI minerals were corrected according to their Åk mole% and TiO_2 wt.% for melilite and fassaite, respectively. The instrumental bias on $\delta^{25}Mg$ in spinel is estimated by assuming the $\delta^{25}Mg$ value in the standard to be 0. Because the standard is very close to pure $MgAl_2O_4$ (0.6 wt.% FeO), we corrected matrix effects on $\delta^{25}Mg$ measurements of spinel in CAIs using data from our spinel standard. External reproducibility (2SD, 2 standard deviation) of measured $\delta^{25}Mg$ values of standard is typically 0.1–0.2‰, which is usually similar to or slightly larger than internal error (2SE, two standard error of the mean of 30 cycles in a single analysis). The final errors of $\delta^{25}Mg$ values in unknown samples are assigned to be the same as the 2SD of bracketing standards, unless internal errors are much larger than the external errors (see Table EA2).

An isotope mass fractionation correction (both instrumental and natural) is applied to the SIMS measured magnesium isotope ratios in order to estimate excess ^{26}Mg. The fractionation-corrected $\delta^{26}Mg^*$ values were calculated using an exponential law with the coefficient $\beta = 0.514$ (Davis et al., 2005) from the evaporation experiments of Richter et al. (2007a).

$$\delta^{26}Mg^* = \delta^{26}Mg - \left[(1 + \delta^{25}Mg/1000)^{1/\beta} - 1\right] \times 1000 \quad (1)$$

External reproducibility of fractionation-corrected $\delta^{26}Mg^*$ values for standards were typically 0.04‰ (2SD) for a fassaite glass standard (FAS-G H5; $TiO_2 = 4.8\%$) and the spinel standard and 0.1‰ (2SD) for the $Åk_{65}$ glass standard, which are comparable to internal errors of individual analyses (2SE). We always see a slight positive offset of measured $\delta^{26}Mg^*$ values at the level of 0.1–0.3‰ for glass and mineral standards, which we attribute to a small instrumental bias, possibly due to the efficiency of the detectors or some other unknown matrix effects. The offset is corrected according to the value obtained from the bracketing standard analyses. For aluminum-rich melilite glass standards ($Åk_{15–25}$), the reproducibility of the standard was degraded to 0.15–0.20‰ due to lower Mg ion intensities, although they are comparable to the internal errors of individual analyses. The errors of the $\delta^{26}Mg^*$ values for unknown melilite analyses were estimated by combining the internal error of each analysis and the error of the average value of eight bracketing $Åk_{65}$ glass standard (i.e., 2SD of standard analyses was divided by $\sqrt{n}$; see Tables EA2-1 and EA2-2). For fassaite glass standards, the $\delta^{26}Mg^*$ values in two standards with lower TiO_2 contents (~2 wt.%) (FAS-G L2 and H2 in Table EA1) are systematically lower than other fassaite glass standards by nearly 0.1‰, so that we applied the second order correction linearly with TiO_2 contents and included an additional 0.05‰ uncertainty that propagated to the final error. We checked $^{48}Ti^{++}$ interference to $^{24}Mg^+$ peak, but the contribution from Ti interference is negligibly small. The second-order corrections for Ti in the CAI fassaite (2.5–8.6 wt.% TiO_2) are less than 0.07‰ (Table EA2-3). For spinel analysis, unknown sample and standard are very similar in chemical composition, so that additional biases from matrix effects are not considered. Therefore, external reproducibility of the average $\delta^{26}Mg^*$ value of bracketing standard (2SD) was applied to the final error assignment (Table EA2-4).

The external reproducibility of the measured $^{27}Al/^{24}Mg$ ratios of the standards was better than 1% (2SD). Relative sensitivity factors (RSF) of $^{27}Al/^{24}Mg$ ratios were calculated by comparing those of raw SIMS data and those calculated from EPMA analyses.

$$RSF = (^{27}Al/^{24}Mg)_{SIMS}/(^{27}Al/^{24}Mg)_{EPMA} \quad (2)$$

For melilite and fassaite analyses, multiple standards with a range of major element concentrations were analyzed to estimate RSF. There is no obvious change in the RSF among melilite standards including both glasses and a synthetic crystal ($Åk_{15–75}$), so that the RSF is estimated to be 0.911 with an uncertainty of 1% for melilite. The RSF in two fassaite glass standards with lower TiO_2 contents (~2 wt.%) were systematically higher than those in other standards (Table EA2-3). It is possible that complex mixtures of major elements in solid solution in fassaite make the RSF more variable than a simple solid solution in melilite. We also applied 1% uncertainty in RSF of spinel analyses (Table EA2-4) due to uncertainties of EPMA calibrations.

2.3.2. Anorthite analyses

For magnesium isotope analysis of anorthite, we used the monocollection electron multiplier (EM) in magnetic peak switching mode, while the $^{27}Al^+$ signal was detected using a multicollection FC detector (with a 10^{11} ohm resistor) on the high mass side simultaneously with the detection of $^{25}Mg^+$. The primary beam intensity was ~1.3 nA with 8 μm oval shaped spots (Fig. 2d), using a mass aperture of 100 μm and beam aperture of 400 μm. Due to the smaller beam size, the field aperture was set to 4000 μm squares and the regular circular mode was used for the coupling optics. The typical $^{24}Mg^+$ and $^{27}Al^+$ ion intensities were $\sim 2 \times 10^5$ and 5×10^7 cps, respectively. The mass resolving power (M/ΔM) was set to 3500 (at 10% peak height) by setting entrance and exit slit widths of 90 and 300 μm, respectively. Other instrumental parameters are the same as those for multicollection FC analyses. A single analysis takes ~30 min, including 400 s of presputtering to stabilize Mg ion intensity, ~60 s for automated centering of the secondary optics, and 50 cycles of switching between $^{24}Mg^+$, $^{25}Mg^+$ and $^{26}Mg^+$ (counting times of 3, 10, and 10 s, respectively, with 3 s waiting time). We used a natural plagioclase mineral standard with An_{59} composition (Lab1), which was previously used as a standard for Al–Mg dating of

Table 1
The Al–Mg isotope analyses of melilite, fassaite, and spinel in Leoville 3535-1 Type B1 CAI.

Analysis number	$^{27}Al/^{24}Mg$	Error[a]	$\delta^{26}Mg^*$ (‰)	Error[a] (‰)	$\delta^{25}Mg$ (‰)	Error[a] (‰)
Session 1 (2007 July)						
Melilite core -#19	1.23	0.01	0.577	0.084	5.52	0.07
Melilite core -#20	1.21	0.01	0.663	0.087	5.53	0.07
Melilite mantle -#21	2.10	0.02	0.805	0.095	5.62	0.07
Melilite mantle -#22	3.99	0.04	1.554	0.102	5.08	0.07
Melilite mantle -#23	6.04	0.06	2.290	0.105	3.66	0.07
Melilite mantle -#24	7.29	0.07	2.719	0.105	5.30	0.07
Melilite mantle -#25	5.94	0.06	2.205	0.101	5.21	0.07
Melilite mantle -#26	7.15	0.07	2.804	0.106	4.45	0.07
Melilite mantle -#27	9.11	0.09	3.243	0.136	3.71	0.07
Session 3 (2009 September)						
Melilite mantle -#41	1.97	0.02	0.780	0.081	5.35	0.12
Melilite mantle -#42	3.76	0.03	1.320	0.095	5.12	0.12
Melilite mantle -#43	1.57	0.01	0.656	0.074	5.61	0.12
Melilite core -#44	1.14	0.01	0.384	0.057	5.07	0.12
Melilite core -#45	1.03	0.01	0.389	0.066	5.15	0.12
Melilite core -#46	1.15	0.01	0.622	0.063	5.36	0.12
Melilite mantle -#47	6.56	0.05	2.367	0.105	4.63	0.12
Melilite mantle -#48	8.22	0.07	2.715	0.131	3.50	0.12
Melilite mantle -#49	2.07	0.02	0.733	0.084	5.10	0.12
Fassaite -#59 ($TiO_2 = 8.0\%$)	2.23	0.11	0.874	0.067	5.09	0.25
Fassaite -#60 ($TiO_2 = 5.5\%$)	1.99	0.10	0.871	0.069	4.79	0.25
Fassaite -#61 ($TiO_2 = 2.8\%$)	1.05	0.05	0.567	0.067	4.34	0.25
Fassaite -#62 ($TiO_2 = 2.5\%$)	1.05	0.05	0.452	0.064	4.45	0.25
Fassaite -#63 ($TiO_2 = 4.2\%$)	1.80	0.09	0.768	0.062	5.08	0.25
Fassaite -#64 ($TiO_2 = 8.6\%$)	2.05	0.10	0.824	0.070	5.17	0.25
Fassaite -#65 ($TiO_2 = 5.1\%$)	1.28	0.06	0.631	0.066	4.86	0.25
Fassaite -#66 ($TiO_2 = 7.6\%$)	2.12	0.11	0.851	0.076	5.07	0.25
Spinel -#47 (fassaite)	2.56	0.03	0.946	0.045	5.76	0.10
Spinel -#48 (melilite mantle)	2.62	0.03	0.899	0.045	5.47	0.12
Spinel -#49 (anorthite)	2.59	0.03	0.886	0.045	6.19	0.11
Spinel -#50 (core)	2.59	0.03	1.083	0.045	5.72	0.11
Spinel -#51 (anorthire in core)	2.60	0.03	0.957	0.045	5.55	0.12
Spinel -#52 (fassaite in core)	2.55	0.03	0.899	0.045	5.50	0.11
Spinel -#53 (fassaite)	2.59	0.03	0.958	0.045	5.96	0.14
Spinel -#54 (spinel aggregates)	2.62	0.03	0.952	0.045	5.93	0.12
Spinel -#55 (spinel aggregate)	2.60	0.03	0.962	0.045	5.66	0.12

[a] Error assigned to individual values are at the 95% confidence level.

chondrules (e.g., Kita et al., 2000; Kurahashi et al., 2008) and has a similar $^{27}Al/^{24}Mg$ ratio (~280) to those in the anorthite of the CAI. Reproducibility of $\delta^{26}Mg^*$ values of the plagioclase standard was better than 1‰, although showing a small negative bias of −1.5‰ that was corrected for in unknown samples (Table EA2-5). The RSF of anorthite is estimated by using measured $^{27}Al/^{24}Mg$ ratios of the Lab1 standard. However, due to its low magnesium contents (~0.1 wt.% MgO), the uncertainty of calibration of the $^{27}Al/^{24}Mg$ ratio using EPMA is as large as 6%. Moreover, the major element composition of Lab1 is more sodium-rich (An_{59}) than the pure anorthite in the CAI, and therefore the RSF may be different from that of the standard.

More recently, a synthetic anorthite glass standard that is doped with 1.0 wt.% MgO ("AnG + Mg 1%") became available for more precise RSF estimates (Kita et al., 2009b). We compared SIMS-measured $^{27}Al/^{24}Mg$ ratios between Lab1 and this anorthite glass standard in three separated Al–Mg sessions in 2009–2010 and found that their ratios were consistent within 1%. Thus, the RSF of anorthite applied to the CAI analyses was reevaluated by using the new anorthite glass standard to be 1.004 ± 0.013 (see detailed calculation in Table EA2-5). Although the $^{27}Al/^{24}Mg$ ratio of AnG + Mg 1% glass is estimated to be 1%, an additional uncertainty based on the comparison of the measured $^{27}Al/^{24}Mg$ ratios between Lab1 and the glass standard of 0.9% (2σ from three sessions) was propagated to the final error estimate. This made the overall uncertainty of the RSF for anorthite to be 1.3% in the present study.

3. RESULTS

3.1. Al–Mg isotope data

The results of the Al–Mg analyses of Leoville 3535-1 Type B1 CAI are shown in Tables 1 and 2. We obtained 18 melilite, eight fassaite, and nine spinel analyses using

Table 2
The Al–Mg isotope analyses of anorthite in Leoville 3535-1 Type B1 CAI.

Analysis number	$^{27}Al/^{24}Mg$	Error[a]	$\delta^{26}Mg^*$ (‰)	Error[a] (‰)	ECF[b]
Normal spots					
Anorthite -#3	233	4	82.5	1.7	0.45
Anorthite -#4	234	4	84.0	2.1	0.66
Anorthite -#5	214.4	1.4	77.3	1.9	0.54
Anorthite -#6	247.4	1.9	88.4	2.0	0.23
Anorthite -#8	234	3	84.2	2.3	0.57
Anorthite -#9	198	3	71.2	2.2	0.47
Anorthite -#10 (rim of #8-9)	366	18	132.2	6.3	0.85
Irregular spots					
Anorthite -#2 (small holes on BSE)	216	10	62.3	6.3	0.46
Anorthite -#7 (many micro-cracks)	173	4	60.1	2.9	0.42

[a] Error assigned to individual values are at the 95% confidence level.
[b] Error correlation factor between $^{27}Al/^{24}Mg$ and $\delta^{26}Mg^*$ values.

multi-FC mode (S1 and S3) and nine anorthite analyses using mono-EM mode (S2). Full SIMS data and EPMA data are found in Tables EA2 and EA3, respectively. The locations of the SIMS analyses are shown in Fig. EA4. Melilite analyses were made in two sessions two years apart, but there are no systematic differences between the two data sets. Data from the first session (S1) contain more mantle melilite data than the second session (S3). The $^{27}Al/^{24}Mg$ ratios of melilite analyses range from 1.0 to 9.1 and correspond to $Åk_{70–20}$, similar to those observed by Richter et al. (2007b) and Knight et al. (2009) for the same CAI. The $^{27}Al/^{24}Mg$ ratios of fassaite analyses show a smaller range of 1–2, which generally correlate with TiO_2 contents. The excess $\delta^{26}Mg^*$ values range from 0.4‰ to 3‰ for melilite and from 0.5‰ to 0.9‰ for fassaite (Table 1). Most of the melilite and all fassaite analyses in the CAI show heavy magnesium isotope enrichments after instrumental bias correction with the $\delta^{25}Mg$ value of ~5‰. The $\delta^{25}Mg$ values of aluminum-rich melilite ($Åk_{\leqslant 30}$) at the rim of the CAIs show slightly lower values (as low as 3.5‰).

The spinel analyses were made in multiple locations and textural contexts in the CAI, including spinel in mantle melilite, in other minerals (anorthite, fassaite, and core melilite), at the boundary of three minerals (#50), and in spinel aggregates. Because the spinel grains in the CAI are close to pure $MgAl_2O_4$, the $^{27}Al/^{24}Mg$ ratios are constant at 2.59 ± 0.05 ($n = 9$, 2SD; Table EA2-4), which corresponds to an atomic ratio of $Al/Mg = 2.04 \pm 0.04$. The excess $\delta^{26}Mg^*$ values are also indistinguishable with an average value of 0.93 ± 0.06‰ (2SD, $n = 8$; Table EA2-4), except for spot #50 that is at the grain boundary of three minerals in the core ($\delta^{26}Mg^* = 1.08 \pm 0.05$ ‰). The $\delta^{25}Mg$ values of spinel analyses show an average of 5.8 ± 0.5‰ (2SD, $n = 9$; Table EA2-4) that is consistent with those of melilite and fassaite, although the $\delta^{25}Mg$ value of the terrestrial spinel standard is not known and assumed to be zero.

The $^{27}Al/^{24}Mg$ ratios of anorthite range from 170 to 370, with most of the data having values of 200–250. The excess $\delta^{26}Mg^*$ values range between 60‰ and 130‰ (Table 2). For most analyses, the $^{27}Al/^{24}Mg$ ratios and $\delta^{26}Mg^*$ values were constant during 50 cycles of analyses of each spot. However, for spot #10, the ^{24}Mg signal intensities fluctuated between 1.1×10^5 and 1.9×10^5 cps, which resulted in the variation of $^{27}Al/^{24}Mg$ ratios between 470 and 280 that correlate with the excess $\delta^{26}Mg^*$ values from 170‰ to 100‰ (Table EA2-6). For this reason, we estimated the error correlation coefficient between $^{27}Al/^{24}Mg$ ratios and the excess $\delta^{26}Mg^*$ values of individual cycles for all the anorthite analyses. As shown in Table 2, the error correlation coefficients were mostly ~0.5 or less, except for spot #10 showing a value of 0.85.

3.2. Al–Mg isochron diagram

The data in Tables 1 and 2 are plotted as an ^{26}Al–^{26}Mg isochron diagram in Fig. 3. A regression of data using ISOPLOT (Ludwig, 2003) yields a well-correlated isochron with a slope of 0.3590 ± 0.0008 (on a $\delta^{26}Mg^*$ vs. $^{27}Al/^{24}Mg$ diagram) with an initial $\delta^{26}Mg^*$ value of 0.06 ± 0.08‰. We rejected two anorthite data (#2 and #7) because they were obviously off the line. In Fig. 4, we compared SEM images of SIMS spots after anorthite analyses and found unusual features on analysis spots #2 and #7, which were rejected from the regression line. The spot #2 contains small dark dotted areas, possibly μm-scale inclusions, and spot #7 show small cracks. In contrast, other spots were featureless and smooth. These two outlier data may have been affected by secondary processes in the parent body, such as impact deformation or shock melting observed from objects in Leoville (e.g., Nakamura et al., 1992; Caillet et al., 1993). The SIMS spots of Mg-rich minerals sometime show a similar minor cracks (EA4), though there are no obvious relationship to their ^{26}Al–^{26}Mg data.

The error associated with the slope of the regression line is only 0.2%, although the uncertainties of anorthite and melilite RSF at the level of 1% should be included when comparing the data with that from other laboratories. The slope corresponds to a $^{26}Al/^{27}Al$ ratio of $(5.002 \pm 0.065) \times 10^{-5}$. The MSWD (Mean Square Weighted Deviation) of the regression line is 5.4, which is significantly larger than unity. As shown in Fig. 3b, the magnesium-rich data closer to the origin of the isochron show a small amount of scatter around the best-fit line (0.1–0.2‰) that is somewhat larger than the analytical uncertainties (~0.05‰).

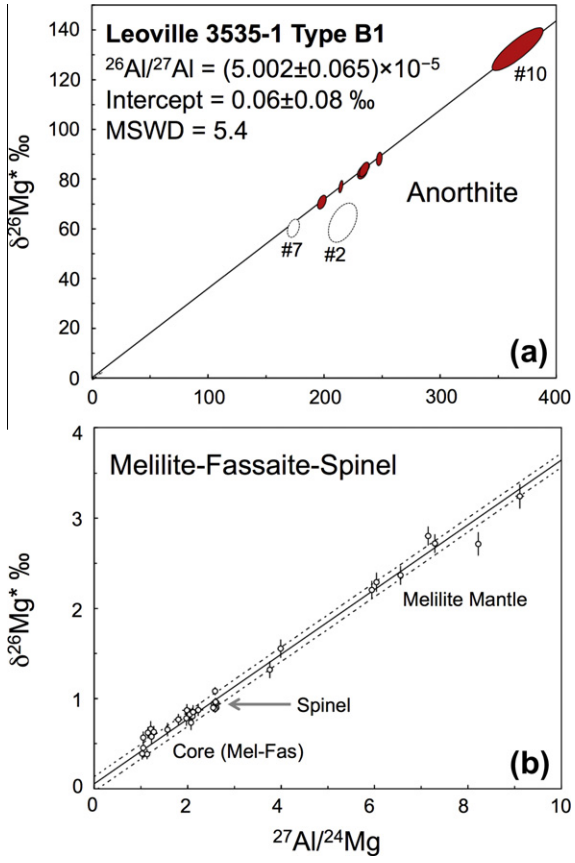

Fig. 3. ^{26}Al–^{26}Mg isochron diagram of Leoville 3535-1. (a) anorthite data, (b) magnesium-rich mineral data. Anorthite data points #2 and #7 are off the linear trend and were not included in the regression determining the slope of the isochron. The dashed line in (b) indicates 2σ error limits of the regression line.

If a kinetic mass fractionation correction with $\beta = 0.511$ (e.g., Young et al., 2002; Bizzarro et al., 2004) is applied instead of $\beta = 0.514$ that was derived from evaporation experiments (Davis et al., 2005), the excess $\delta^{26}Mg^*$ values would be lower by 0.06‰ for a sample with $\delta^{25}Mg = 5‰$. Because most data have very similar $\delta^{25}Mg$ (5–6‰), using $\beta = 0.511$ would shift the regression line parallel to the one shown in Fig. 3. This would lower the initial $\delta^{26}Mg^*$ value to $0.00 \pm 0.08‰$, but the slope of the isochron would not change. Data from the aluminum-rich melilite rim have slightly lower $\delta^{25}Mg$ values of 3–4‰ and the excess $\delta^{26}Mg^*$ values using kinetic mass fractionation law would shift the data by only 0.03–0.04‰, which is much smaller than their analytical uncertainties. In fact, the isochron slope estimated from our SIMS data is strongly controlled by the anorthite data with excess $\delta^{26}Mg^*$ values of 70–130‰.

3.3. Anorthite rim with low Mg content

In this study, three analyses were made from a single anorthite grain (spots #8–10, Fig. 5a) to evaluate subsolidus magnesium isotope diffusion effects that might have disturbed or reset the Al–Mg isotope system (e.g., LaTourrette and Wasserburg, 1998). We intentionally aimed one spot at the rim of the grain within 10 μm of the boundary adjacent to melilite (spot #10). The $^{27}Al/^{24}Mg$ ratio of #10 was the highest among all the analyses in the CAI and the ratio varied from 280 to 470 during the 50 cycles of analyses (Fig. 5b). The result indicates a heterogeneous distribution of magnesium in the anorthite at a scale smaller than the depth sampled by a single analysis (~1 μm). If there were subsolidus reheating events for the CAI after the solidification of anorthite, the excess ^{26}Mg that had been accumulated in anorthite would be modified by isotope exchange with isotopically normal magnesium during diffusion. The magnesium-poor domain of spot #10 should be the first place to see such an effect, because it is close to the grain boundary of an otherwise magnesium-rich mineral and has a low magnesium concentration. For this reason, we calculated the average $^{27}Al/^{24}Mg$ ratio and $\delta^{26}Mg^*$ value from cycles 27–36 of spot #10, where the ^{24}Mg intensities were lowest (Fig. 5b and c and Table EA2-6). The average value from the low magnesium cycles of spot #10 (here after called #10L) plots exactly on the same isochron with other data (Fig. 5d). The model initial $^{26}Al/^{27}Al$ ratio of the #10L is calculated to be $(5.1 \pm 0.2) \times 10^{-5}$, which agrees with the internal isochron of the CAI within error. The error of the model $^{26}Al/^{27}Al$ ratio (precision ~4%) corresponds to uncertainty of ~40 ka in relative age. Thus, anorthite in Leoville 3535-1 does not show any evidence of subsolidus reheating postdating the crystallization of the CAI by more than 40 ka.

4. DISCUSSION

4.1. Relative age of the Leoville 3535-1 Type B1 CAI

The internal ^{26}Al–^{26}Mg isochron of CAI Leoville 3535-1 is interpreted to represent the time when the minerals in this CAI crystallized from a melt. If the initial $^{26}Al/^{27}Al$ ratio of the Solar System was homogeneous, the relative formation time (Δt) is estimated by Eq. (3).

$$\Delta t = -\tau \times \ln\left[\frac{(^{26}Al/^{27}Al)_{L3535\text{-}1}}{(^{26}Al/^{27}Mg)_{SSI}}\right] \quad (3)$$

In the above equation, mean life τ is 1.02 Ma using the ^{26}Al half-life of 0.705 Ma (Norris et al., 1983) and the $(^{26}Al/^{27}Al)_{SSI}$ is the Solar System Initial (SSI) $(^{26}Al/^{27}Al)$ ratio. It is often assumed that the bulk CAI ^{26}Al–^{26}Mg isochron represents the time when refractory solids first condensed from a well-mixed gas of solar composition, giving a range of Al/Mg ratios among bulk CAIs. Thus, the relative time Δt is calculated relative to the time of bulk CAI isochron. Multiple bulk CAIs analyses made by Thrane et al. (2006) and Jacobsen et al. (2008) both show well-correlated ^{26}Al–^{26}Mg regression lines, but their inferred initial $^{26}Al/^{27}Al$ ratios differ by 11%, which is much larger than their reported uncertainty. Thrane et al. (2006) reported an initial $^{26}Al/^{27}Al$ ratio of $(5.85 \pm 0.05) \times 10^{-5}$, while Jacobsen et al. (2008) reported an initial $^{26}Al/^{27}Al$ ratio of $(5.23 \pm 0.13) \times 10^{-5}$. Recently, Larsen et al. (2011) reported a new result from bulk CAI-AOAs $^{26}Al/^{27}Al$ ratio of $(5.25 \pm 0.02) \times 10^{-5}$ that was obtained in the same laboratory of Thrane et al. (2006). Thus, the discrepancy

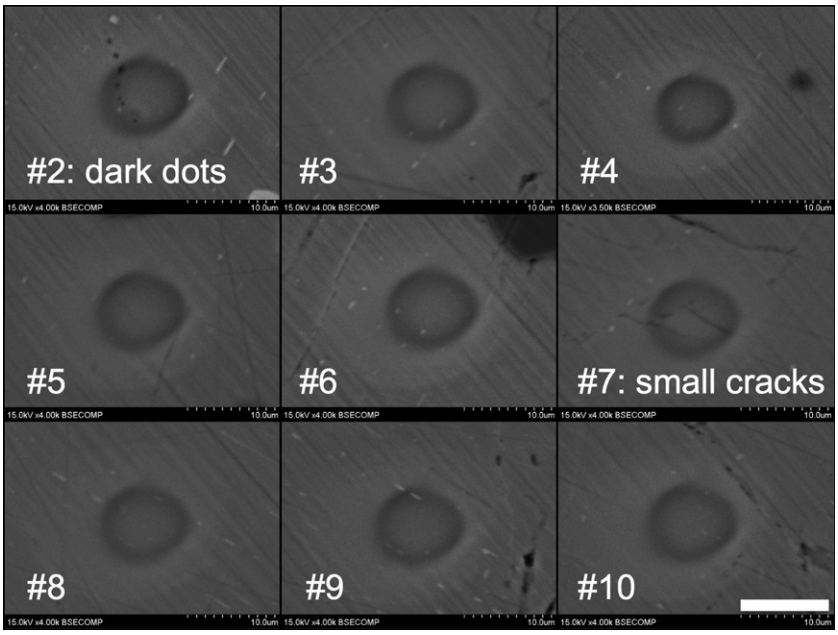

Fig. 4. BSE images used to examine the SIMS pits that were produced by the anorthite analyses. The two data points that are off the regression line in Fig. 3 (#2 and #7) have irregular SIMS pits, indicating possible disturbance by secondary processes in the parent body. The scale bar is 10 μm long. Fine lines on the diagonal directions seen in all images are scratches from polishing.

between two groups seems to be resolved. Another independent investigation by Baker (2008) also supports the value obtained by Jacobsen et al. (2008).

MacPherson et al. (2010, 2012) reported ^{26}Al–^{26}Mg isochron data from two pristine fine-grained type A (FTA) CAIs with the initial ^{26}Al/^{27}Al ratios of $(5.27 \pm 0.17) \times 10^{-5}$ and $(5.29 \pm 0.28) \times 10^{-5}$, which may represent the formation of earliest condensates in the solar nebula. These values are in agreement with those of the bulk CAI isochrons by Jacobsen et al. (2008) and Larsen et al. (2011), supporting that the initial ^{26}Al/^{27}Al ratios of the bulk CAIs represent the formation of earliest condensates in the solar nebula.

Several in-situ ^{26}Al–^{26}Mg studies using both LA-ICP-MS and MC-SIMS suggested evidence for "supra-canonical" ^{26}Al/^{27}Al ratios (Taylor et al., 2005; Young et al., 2005; Cosarinsky et al., 2007; Connolly et al., 2009, 2010). Connolly et al. (2009) compared the analyses of a single CAI by using both LA-ICP-MS and SIMS and found consistent results between the two methods. Therefore, the elevated ^{26}Al/^{27}Al ratios are not analytical artifacts. However, all these data reporting supra-canonical ^{26}Al/^{27}Al ratios were not derived from CAIs with well-defined ^{26}Al–^{26}Mg isochron regression. Considering that the bulk CAI isochrons by several groups now consistently show canonical initial ^{26}Al/^{27}Al ratios, it is very unlikely that individual CAIs formed originally with ^{26}Al/^{27}Al ratios higher than bulk data, unless there were complex isotope exchange in open system as proposed by Simon and Young (2011). Rather, elevated ^{26}Al/^{27}Al ratios might be estimated from data points that plot above the bulk CAI isochron as a result of later redistribution of ^{26}Al–^{26}Mg system.

Here, we use the initial ^{26}Al/^{27}Al ratios of the bulk CAIs for substituting that of SSI in the Eq. (3). The relative ages $\Delta t = 46 \pm 29$ and 50 ± 13 ka are obtained using the bulk CAI isochron data of Jacobsen et al. (2008) and Larsen et al. (2011), respectively. Thus, the final crystallization of Leoville 3535-1 Type B1 CAI postdates the time given by the bulk CAI isochron by ~50 ka.

4.2. Internal Al–Mg isotope systematics in Leoville 3535-1

4.2.1. Closure of the Al–Mg system in anorthite

In this work, a very precise initial ^{26}Al/^{27}Al ratio was obtained because of well-correlated isochron data from anorthite with extremely radiogenic magnesium isotope ratios ($\delta^{26}Mg^* = 70$–$130‰$). According to crystallization experiments for Type B CAI compositions (MacPherson et al., 1984; Stolper and Paque, 1986), spinel and melilite crystallize before fassaite and anorthite. Type B CAIs often show a reverse-zoned melilite mantle, indicative of crystallization of fassaite prior to anorthite, which requires cooling rates faster than ~0.5 °C h^{-1} (MacPherson et al., 1984). The texture of Type B CAIs with coarse fassaite and anorthite indicates nearly synchronous crystallization of these minerals under the cooling rates <50 °C h^{-1} (Stolper and Paque, 1986). Thus, anorthite is among the last minerals to crystallize in type B CAIs and the inferred initial ^{26}Al/^{27}Al ratio obtained in this study most likely represents the time of last melting of the CAI.

Alternatively, the CAI might experience resetting of ^{26}Al–^{26}Mg system by later subsolidus heating. Anorthite is especially sensitive to disturbance, because magnesium diffusion in anorthite is faster than in other CAI minerals

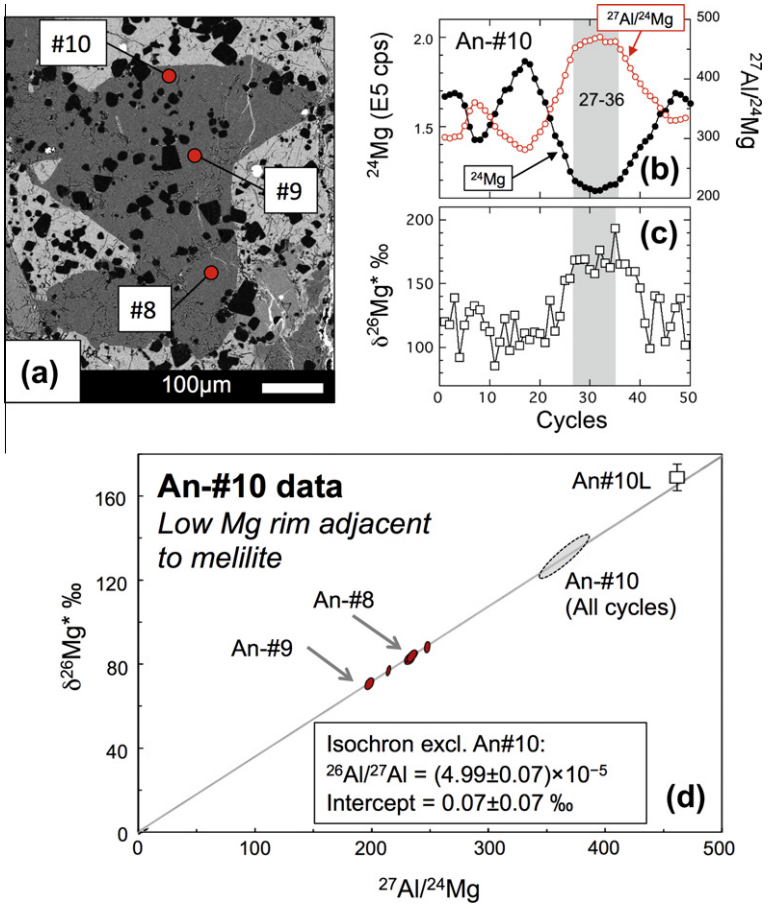

Fig. 5. An anorthite analysis at the rim adjacent to melilite (#10). (a) Location of analyses. Two other spots (#8 and #9) were obtained in the same grain near the center. (b) Variation of ^{24}Mg intensity and $^{27}Al/^{24}Mg$ ratios within a single analysis (50 cycles). Cycles 27–36 (shown as grey) show the highest $^{27}Al/^{24}Mg$ ratios. (c) The excess $\delta^{26}Mg^*$ of individual cycles, showing highest values at cycles 27–36. (d) The average data from cycles 27–36 of the analysis #10 ("An#10L") plot on the isochron diagram. The two other spots in the same anorthite grain (#8 and #9) have lower $^{27}Al/^{24}Mg$ ratios similar to other analyzed anorthite grains. The grey line represents a regression line of all data excluding anorthite #10, which is indistinguishable from the isochron shown in Fig. 3. The data for An#10L plot on the same isochron as the rest of data. The average of all 50 cycles of spot #10 (An-#10) is shown as an error ellipse for comparison.

(LaTourrette and Wasserburg, 1998; Liermann and Ganguly, 2002; Ito and Ganguly, 2009). Diffusion could have affected the magnesium isotopic composition and/or the Al/Mg ratio during subsolidus reheating events in the solar nebula (e.g., Young et al., 2005; Ito and Messenger, 2010; Simon and Young, 2011) or during parent body thermal metamorphism. The analysis obtained from the rim of an anorthite grain adjacent to melilite (An-#10) shows excellent agreement with rest of the anorthite analyses, even though the magnesium concentration in the spot was the lowest among all the analyses and variable within the analytical depth of ~1 μm. Low and variable magnesium contents in the An-#10 analysis could be caused by a redistribution of magnesium postdating the last melting event (Yurimoto et al., 2000), although it must have taken place shortly after the final crystallization of anorthite such that the isochron was not affected. Thus, the Leoville 3535-1 anorthite data strongly indicate the absence of subsolidus diffusion over a prolonged period since the last melting of the CAI.

Ito and Ganguly (2009) compared diffusion rates of magnesium among anorthite, spinel, and melilite and concluded that melilite should be the most robust phase for Al–Mg dating of CAIs. MacPherson et al. (2012) found spinel grains that show large ^{26}Mg excesses up to 3‰ in a Vigarano F1 type B CAI. The large excess is found exclusively for spinel grains included in anorthite, in which ^{26}Mg excesses were nearly completely erased by later parent body alteration associated with the formation of nepheline lamellae. In contrast, analyses of spinel grains in melilite and fassaite in the same CAI plot along the isochron defined by melilite and fassaite with the canonical $^{26}Al/^{27}Al$ ratio. MacPherson et al. (2012) explained unsupported excess ^{26}Mg in spinel surrounded by anorthite as a result of isotope exchange between anorthite and spinel by a subsolidus heating event due to fast diffusion of magnesium in these minerals, while spinel in melilite and fassaite did not exchange magnesium with host mineral due to slow diffusion rate of magnesium in the host.

In contrast to Vigarano F1, we do not find any difference among spinel data that are hosted by anorthite, melilite and fassaite in Leoville 3535-1. Anorthite in the CAI is unaltered and does not show thin lamellae of nepheline.

Therefore, there is no indication of subsolidus heating events that could modify the ^{26}Al–^{26}Mg system of the Leoville 3535-1. Similarly, the internal ^{26}Al–^{26}Mg systematics of Leoville 3535-1 CAI and the data collected closest to the rim does not support this CAI being affected by subsolidus heating events in the solar nebula that lasted for a time as long as 0.3 Ma suggested by Young et al. (2005).

4.2.2. Multiple melting process

While we find the well-defined correlated excess from anorthite data, the MSWD of the isochron fit of all data (~5) is significantly larger than unity, indicating a multi-stage evolution of the ^{26}Al–^{26}Mg system. Fig. 6 shows an expanded view of isochron diagram at magnesium-rich end. Data scatter significantly beyond analytical uncertainties along the isochron regression line, which results in the large MSWD. There seems to be systematic displacement from the regression line depending on mineral phases. Spinel data, except for one spot, plot below the regression line, while fassaite data plot above the line. Melilite data plot generally on or below the line similar to spinel, but some of most åkermanite-rich melilite plot above the line, similar to fassaite.

The coarse-grained texture of Leoville 3535-1 indicates that it was almost completely melted and cooled slowly, no more that a few tens degrees per hour. The melilite is zoned with increasing åkermanite towards the interior, which indicates that the mantle crystallized inwards from the rim, similar to what was observed experimentally when CAI-like melts were heated under extremely reducing conditions (Mendybaev et al., 2006). Stolper and Paque (1986) used experimental data to argue that heating of Type B CAIs produced a high degree of partial melting with some fraction of the original spinel having remained solid while other minerals melted; melilite, fassaite and anorthite crystallized as the melt cooled. Because some fraction of the spinel might predate the melting event and because virtually all the melilite would have crystallized before fassaite and anorthite, we calculated a regression line made by the fassaite and anorthite data. As shown in Fig. 7, the regression line shows MSWD nearly unity and the inferred initial $^{26}Al/^{27}Al$ ratio of $(4.988 \pm 0.065) \times 10^{-5}$ with a positive intercept of $\delta^{26}Mg^* = 0.13 \pm 0.03‰$. The inferred initial $^{26}Al/^{27}Al$ ratio is indistinguishable from that obtained by all data in Fig. 3. Several åkermanitic melilite and one spinel data also plot along the line. The åkermanitic nature of these core melilites indicates that they were the last melilites to crystallize, which would have been at much the same as when fassaite and anorthite would have begun to crystallize. Thus, it is not entirely surprising that the core melilites plot along with the fassaite data. One spinel analysis plots on the fassaite-anorthite isochron (#50) located at the boundary of multiple minerals in the core of the CAI (Fig. EA4-6). Magnesium isotopes in spinel #50 would have equilibrated with fassaite and anorthite during the last melting event. In contrast, other spinel data plot below the fassaite-anorthite line, which is consistent with the idea that spinel remained solid during the last melting event. Gehlenitic melilite in the melilite mantle could also have remained solid during the last melting. However, relatively larger analytical errors on aluminum-rich melilite do not allow us to resolve any potential differences.

Mass dependent fractionations of magnesium isotopes in spinel (as indicated from $\delta^{25}Mg$ values) are almost identical to those in melilite and fassaite and positively fractionated by ~5‰ (Table 1). Because the excess $\delta^{26}Mg^*$ in spinel might not have been homogenized with the melt during the last melting event, heavy isotope enrichment of Mg would have originated from earlier heating events predating the fassaite–melilite isochron. Such events could include nearly complete melting of the CAI precursor, in which spinel had crystallized. Alternatively, solid precursors of the CAI already acquired heavy magnesium enrichment by earlier evaporation processes. In either case, the magnesium isotope exchange between molten CAI and surrounding nebula gas might not occur significantly during the last melting event. Minor magnesium isotope exchange would have occurred at the rim of melilite mantle that show systematically lower $\delta^{25}Mg$ values (Richter et al., 2007b; Knight et al., 2009). High precision Al–Mg dating of

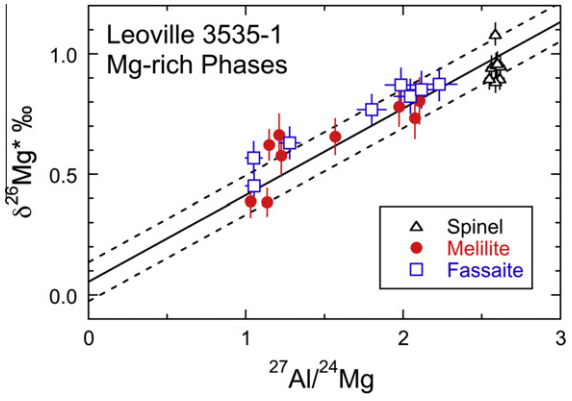

Fig. 6. Comparison of ^{26}Al–^{26}Mg data for spinel, melilite, and fassaite with low $^{27}Al/^{24}Mg$ ratios (<3). The solid and dashed lines are the regression line and error limits shown in Fig. 3b. Data show significant scatter and some data are displaced beyond analytical uncertainties. Generally, the spinel data and the fassaite data plot below and above and the regression line, respectively, even though most data fall on the regression line within errors.

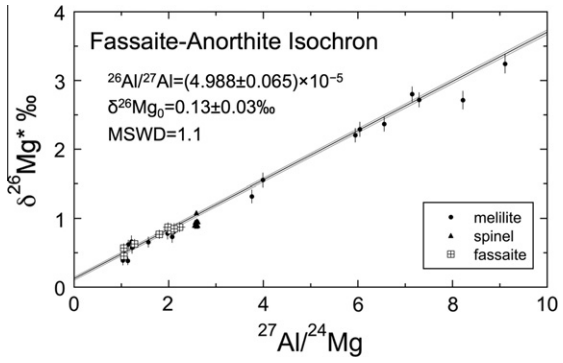

Fig. 7. The ^{26}Al–^{26}Mg isochron for fassaite-anorthite data. Anorthite data are not shown in this figure, but melilite and spinel data are shown as filled symbols in comparison. The best fit line and error envelopes are shown as black and grey lines, respectively.

several Vigarano CAIs (MacPherson et al., 2012) also indicates similar closed system evolution of magnesium isotopes during the reheating of CAIs (Davis et al., 2010).

If anorthite last crystallized during a later reheating event while spinel (and potentially some melilite) remained solid and preserved the isotopic signature of the initial crystallization event, the regression line made by fassaite-anorthite would provide the better estimate of the initial $^{26}Al/^{27}Al$ ratios characteristic of the last partial melting event. Compared to the inferred $^{26}Al/^{27}Al$ ratio of $(5.002 \pm 0.065) \times 10^{-5}$ using all data (Fig. 3), the value of $(4.988 \pm 0.065) \times 10^{-5}$ obtained from fassaite-anorthite regression line is lower only by 0.3% and thus the difference between two regression lines is insignificant. Since the multiple melting processes in Type B1 CAI could be very complicated, we consider the regression line using all data as the best estimate of initial $^{26}Al/^{27}Al$ ratio of the Leoville 3535-1 CAI, but we recognize that it is dominated by data points affected by the later reheating event, especially those in anorthite.

4.2.3. Positive intercept of ^{26}Al–^{26}Mg isochron regression

The intercept of isochron regressions in Fig. 3 (all data) and Fig. 7 (fassaite–anorthite) show positive $\delta^{26}Mg^*$ values of $0.06 \pm 0.08‰$ and $0.13 \pm 0.03‰$, respectively, while the former value can not be distinguished from zero beyond the statistical uncertainty. As mentioned earlier, these values might be systematically decreased by 0.06‰ if $\beta = 0.511$ (kinetic mass fractionation) is used for the mass dependent fractionation correction law. In either correction methods, fassaite-anorthite regression line shows a positive intercept beyond analytical uncertainties, which may indicate the internal redistribution of radiogenic ^{26}Mg in the CAI during the last melting event. The difference between initial $\delta^{26}Mg^*$ values of fassaite–anorthite isochron of Leoville 3535-1 and bulk CAI isochron data are $0.11 \pm 0.04‰$ and $0.13 \pm 0.05‰$, by applying the intercepts of bulk isochron data from Jacobsen et al. (2008) corrected for $\beta = 0.511$ and 0.514, respectively ($-0.040 \pm 0.029‰$ and $-0.004 \pm 0.044‰$). The small increase of $\delta^{26}Mg^*$ values at ~0.1‰ may be explained by the closed system evolution of ^{26}Al–^{26}Mg system for the first 50 ka under the $^{27}Al/^{24}Mg$ ratio of ~7, which is significantly higher than those of bulk Type B CAIs (2.2-3, Jacobsen et al., 2008). It is possible that the partial melt was enriched in Al_2O_3 relative to MgO by selective melting of anorthite during reheating processes of the CAI. However, it is difficult to model the detail growth of $\delta^{26}Mg^*$ values in the CAI, given the relatively large uncertainties of analyses.

4.3. Implications for the early history of the solar nebula

In Fig. 8, the initial $^{26}Al/^{27}Al$ ratio of Leoville 3535-1 is compared to the ratios of other type B CAIs from CV3 chondrites from recent internal MC-ICPMS and MC-SIMS analyses with well-defined isochron (Jacobsen et al., 2008; Bouvier and Wadhwa, 2010; MacPherson et al., 2012). Four data are from ICP analyses of mineral separates from Allende CAIs (A44A, AJEF, and A43; Jacobsen et al., 2008) and NWA 2364 (Bouvier and Wadhwa, 2010). Another is from SIMS analyses of the Vigarano Type B2 CAI F1 that was analyzed during the session S3 of this study (MacPherson et al., 2012). Uncertainties of the inferred $^{26}Al/^{27}Al$ ratios of these data are much larger (4–8%) than the present work (1.3%) due to the limited range of $^{27}Al/^{24}Mg$ ratios (typically 2–8) from mineral separates for ICPMS analyses and magnesium-rich minerals for SIMS analyses. In the case of F1, the isochron regression was made using only magnesium-rich minerals due to the anorthite data having been affected by low temperature parent body alteration (MacPherson et al., 2012). The Leoville 3535-1 data agree very well with three Type B CAIs (A44A, AJEF, and NWA 2364) showing the initial $^{26}Al/^{27}Al$ ratios of 5.0×10^{-5}, which is systematically lower than those obtained from the bulk CAI isochron data (Jacobsen et al., 2008; Larsen et al., 2011). Thus, major melting (or remelting) events of refractory solids in the solar nebula that formed Type B CAIs may postdate by ~50 ka the condensation of their solid precursors. Two other Type B CAI (F1 and A43) show initial $^{26}Al/^{27}Al$ ratios lower than that of Leoville 3535-1. These relatively younger Type B CAIs may indicate that heating events affecting the Type B CAIs continued for at least another 0.1 Ma.

A comprehensive study of the Al–Mg system in pristine, unaltered CAIs from Vigarano was undertaken by MacPherson et al. (2012) that included FTA, CTA (compact type A), Type B, Type C and AOAs. They found a systematic

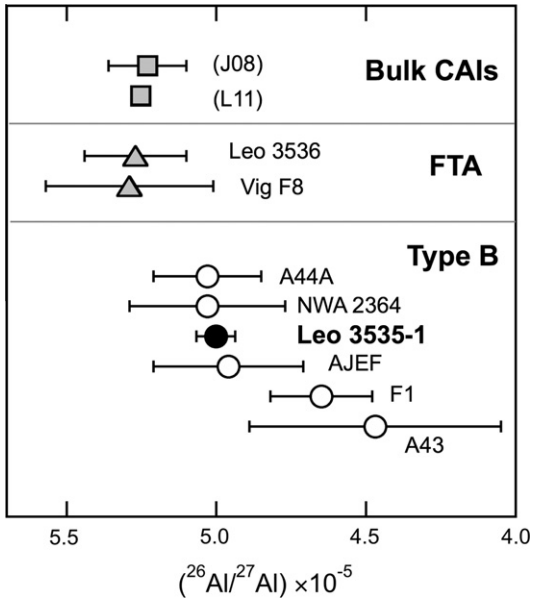

Fig. 8. A compilation of the initial $^{26}Al/^{27}Al$ ratios of individual Type B CAIs from internal isochron regressions. Bulk CAI isochron data from Jacobsen et al. (2008; J08) and Larsen et al. (2011; L11) are shown as reference. Data for Leoville 3535-1 are from Fig. 3. Data sources for the other Type B CAIs: Allende A44, AJEF, and A43 (Jacobsen et al., 2008); NWA 2364 (Bouvier and Wadhwa, 2010); Vigarano F1 (MacPherson et al., 2012). The bulk CAI isochron of Jacobsen et al. (2008) and the internal isochrons of two fluffy Type A CAIs (FTA MacPherson et al., 2010, 2012) suggest systematically higher initial $^{26}Al/^{27}Al$ ratios than Type B CAIs.

difference in the inferred $^{26}Al/^{27}Al$ ratios between unmelted and melted CAIs. Melted CAIs generally show a range of $^{26}Al/^{27}Al$ ratios $(4–5) \times 10^{-5}$ and one unusual Type C CAI contains a subregion with the $^{26}Al/^{27}Al$ ratio 2×10^{-5}, which postdates the bulk CAI isochron by ~1 Ma. Variable initial $^{26}Al/^{27}Al$ ratios within a single CAI have also been found in Allende type B CAI USMN 5241 (Hsu et al., 2000). Therefore, melting of CAIs appears to have continued for as long as 1 Ma, which brings it close to the age of the earliest chondrule formation events.

The time scales for the initial condensation of CAI precursors and their subsequent reheating are comparable to the infalling and evolved protostar stages of low mass stars, known as Class 0 and Class 1 objects, with typical durations of ~10 ka and ~0.1 Ma, respectively (Feigelson and Montmerle, 1999). During these periods, the accretion rate of circumstellar material to the young Sun was high and molecular bipolar flow was active, which would cause high temperature heating events consistent with the chemical and isotopic properties of CAIs (e.g., MacPherson et al., 2005). Ciesla (2010) recently argued that the short interval among ages of CAIs relates to the preservation mechanism of refractory objects in the protoplanetary disk. The refractory inclusions that formed early in the inner disk might spread to the outer disk within the first 0.1 Ma, while those formed in a later period would not be efficiently transported to the outer disk. The early-formed CAIs that were spread over the large heliocentric distances might survive until the time of chondrule formation ($\geqslant$2 Ma) and subsequent planetesimal formation. According to Ciesla's model, the age distribution of CAIs would have a sharp peak at the oldest end. Current available data on type B CAIs show a peak on $^{26}Al/^{27}Al$ $\sim 5.0 \times 10^{-5}$, which corresponds to ~50 ka after the time of bulk CAI isochron (Fig. 8). There are compound CAI–chondrule objects, in which relict CAIs are enclosed by chondrules, showing relatively low initial $^{26}Al/^{27}Al$ ratios (e.g., Makide et al., 2009). These CAI–chondrule compound objects indicate that the CAIs were incorporated to chondrule forming environments more than 2 Ma after CAI forming events. Because the Leoville 3535-1 CAI preserved such a well-defined isochron with $^{26}Al/^{27}Al = 5.0 \times 10^{-5}$, this particular CAI would not have experienced the reheating 2 Ma later during chondrule formation. Pristine CAIs could have been located in parts of the disk where chondrule formation process was not efficient, but were eventually incorporated into the CV chondrite parent body. More analyses of various types of pristine CAIs by in-situ high precision SIMS technique will help to better constrain the environments of their formation, the nature of energetic processes that reheated them and the transport of solid in the protoplanetary disk.

5. CONCLUSIONS

High-precision SIMS ^{26}Al–^{26}Mg analyses of the pristine Type B1 CAI Leoville 3535-1 show a well-defined isochron with the initial $^{26}Al/^{27}Al = (5.002 \pm 0.065) \times 10^{-5}$. Analysis of anorthite near the boundary with melilite shows variable $^{27}Al/^{24}Mg$ ratios of 280–470 and yet plot exactly on the same isochron. We conclude that the CAI did not experience subsolidus diffusion affecting the Al–Mg system much after the last melting event. Assuming a homogeneous distribution of ^{26}Al in the solar system, the Leoville 3535-1 Type B1 CAI last melted ~50 ka after the time of the bulk CAI isochron, most likely the time of condensation of refractory solids in the earliest solar nebula. A small (~0.1‰) scatter of the magnesium isotope ratios from the regression line is observed in magnesium-rich minerals, especially spinel and fassaite being below and above the regression line, respectively. Spinel could be solid residues that survived the partial melting of the CAI precursor, while fassaite and anorthite crystallized from the melt generated by partial melting. Assuming later partial melting and recrystallization of fassaite and anorthite, the isochron regression line was obtained for fassaite-anorthite data with an initial $^{26}Al/^{27}Al$ value of $(4.988 \pm 0.065) \times 10^{-5}$, which is indistinguishable from that obtained from all data. The mass dependent fractionation of magnesium in spinel is almost the same as that in melilite and fassaite, indicating that spinel would have been crystallized during the earlier melting event and that the CAI remained closed against magnesium isotope exchange with solar nebula.

Highly precise and accurate SIMS Al–Mg isotope analysis of CAIs is a powerful means of resolving relative time differences of their formation as short as 10 ka. More studies on a variety of pristine CAIs combining petrographic, chemical, and isotope analyses will provide valuable insights into the earliest history of the Solar System on time scales of 0.1 Ma or less.

ACKNOWLEDGEMENTS

We thank Glenn MacPherson, Smithsonian Institute, for the use of the Leoville 3535-1 sections and helpful discussions. Shigeko Togashi, Geological Survey of Japan-AIST, provided us a plagioclase standard for the Al–Mg analyses. Brian Hess and Jim Kern are acknowledged for preparation of SIMS standard mounts and technical assistance to SIMS operations, respectively. Constructive comments by Justin Simon, Motoo Ito, Joel Baker, and the Associate Editor Sara Russell significantly improved the quality of the manuscript. This work is supported by NASA Cosmochemistry Program (NNX07AI46G, N.K.; NNX09AG38G, F.M.R.; NNX09AG39G, A.M.D.) and NASA Origins of the Solar Systems Program (NNX09AB88G; N.K.). WiscSIMS is partly supported by NSF (EAR03-19230, EAR07-44079).

APPENDIX A. SUPPLEMENTARY DATA

Supplementary data associated with this article can be found, in the online version, at http://dx.doi.org/10.1016/j.gca.2012.02.015.

REFERENCES

Amelin Y., Krot A. N., Hutcheon I. D. and Ulyanov A. A. (2002) Lead isotopic ages of chondrules and calcium–aluminum-rich inclusions. *Science* **297**, 1678–1683.

Amelin Y., Kaltenbach A., Iizuka T., Stirling C. G., Ireland T. R., Peatev M. and Jacobsen S. B. (2010) U–Pb chronology of the Solar System's oldest solids with variable $^{238}U/^{235}U$. *Earth Planet. Sci. Lett.* **300**, 343–350.

Baker J. A. (2008) High-precision ^{26}Al–^{26}Mg dating solid and planetesimal formation in the young Solar System. *Geochim. Cosmochim. Acta Suppl.* **72**, A45.

Bizzarro M., Baker J. A. and Haack H. (2004) Mg isotope evidence for contemporaneous formation of chondrules and refractory inclusions. *Nature* **431**, 275–278.

Bizzarro M., Baker J. A. and Haack H. (2005) Corrigendum: Mg isotope evidence for contemporaneous formation of chondrules and refractory inclusions. *Nature* **435**, 1280.

Bouvier A. and Wadhwa M. (2010) The age of the Solar System redefined by the oldest Pb–Pb age of a meteoritic inclusion. *Nat. Geosci.* **3**, 637–641.

Caillet C., MacPherson G. J. and Zinner E. K. (1993) Petrologic and Al–Mg isotopic clues to the accretion of two refractory inclusions onto the Leoville parent body – one was hot, the other wasn't. *Geochim. Cosmochim. Acta* **57**, 4725–4743.

Catanzaro E. J., Murphy T. J., Garner E. L. and Shields W. R. (1966) Absolute isotopic abundance ratios and atomic weights of magnesium. *J. Res. Natl. Bur. Stand.* **70a**, 453–458.

Ciesla F. J. (2007) Outward transport of high-temperature materials around the midplane of the solar nebula. *Science* **318**, 613–615.

Ciesla F. J. (2010) The distributions and ages of refractory objects in the solar nebula. *Icarus* **208**, 455–467.

Clayton R. N., Grossman L. and Mayeda T. K. (1973) A component of primitive nuclear composition in carbonaceous meteorites. *Science* **182**, 485–488.

Connelly J. N., Amelin Y., Krot A. N. and Bizzarro M. (2008) Chronology of the solar system's first solids. *Astrophys. J.* **675**, L121–L124.

Connolly, Jr., H. C., Young E. D., Huss G. R., Nagashima K., McDonough W. F., Ash R. D., Beckett J. R., Tonui E. and McCoy T. J. (2009) Supra-canonical ^{26}Al detected by in situ LA-MC-ICPMS and SIMS techniques: but what does it all mean? *Lunar Planet. Sci.* **40**, #1993.

Connolly, Jr., H. C., Young E. D., Huss G. R., Nagashima K., Beckett J. R. and McCoy T. J. (2010) To be or not to be canonical, what's new? The search for the initial ^{26}Al abundance of the solar system. *Lunar Planet. Sci.* **41**, #1933.

Cosarinsky M., Taylor D. J., Liu M. C., McKeegan K. D. and Krot A. N. (2007) Distribution of Aluminum-26 in refractory inclusions from CV chondrites. *LPI Contribution No. 1374*, 48–49.

Cuzzi J. N., Davis S. S. and Dobrovolskis A. R. (2003) Blowing in the wind. II. Creation and redistribution of refractory inclusions in a turbulent protoplanetary nebula. *Icarus* **166**, 385–402.

Davis A. M., Richter F. M., Mendybaev R. A., Janney P. E., Wadhwa M. and McKeegan K. D. (2005) Isotopic mass fractionation laws and the initial solar system ^{26}Al/27Al ratio. *Lunar Planet. Sci.* **36**, #2334.

Davis A. M., Kita N. T., Ushikubo T., MacPherson G. J., Bullock E. S. and Knight K. B. (2010) Magnesium isotopic evolution of CAIs. *Lunar Planet. Sci.* **41**, #2496.

De Chambost E., Schuhmacher M., Lovestam G. and Claesson S. (1997) Achieving high transmission with the Cameca IMS 1270. In *Secondary Ion Mass Spectrometry* (eds. A. Benninghoven, B. B. Hagenhoff and H. W. Werner). John Wiley & Sons, New York, pp. 1003–1006.

Fagan T. J., Guan Y. and MacPherson G. J. (2007) Al–Mg isotopic evidence for episodic alteration of Ca–Al-rich inclusions from Allende. *Meteorit. Planet. Sci.* **42**, 1221–1240.

Fahey A. J., Goswami J. N., McKeegan K. D. and Zinner E. (1987) ^{26}Al, ^{244}Pu, ^{50}Ti, REE, and trace element abundances in hibonite grains from CM and CV meteorites. *Geochim. Cosmochim. Acta* **51**, 329–350.

Feigelson E. D. and Montmerle T. (1999) High-energy processes in young stellar objects. *Annu. Rev. Astron. Astrophys.* **37**, 363–408.

Hsu W., Wasserburg G. J. and Huss G. R. (2000) High time resolution by use of the ^{26}Al chronometer in the multistage formation of a CAI. *Earth Planet. Sci. Lett.* **182**, 15–29.

Ireland T. R. (1988) Correlated morphological, chemical, and isotopic characteristics of hibonites from the Murchison carbonaceous chondrite. *Geochim. Cosmochim. Acta* **52**, 2827–2839.

Ito M. and Ganguly J. (2009) Mg diffusion in minerals in CAIs: new experimental data for melilites and implications for the Al–Mg chronometer and thermal history of CAIs. *Lunar Planet. Sci.* **40**, #1753.

Ito M. and Messenger S. (2010) Thermal metamorphic history of a Ca, Al-rich inclusion constrained by high spatial resolution Mg isotopic measurements with NanoSIMS 50L. *Meteorit. Planet. Sci.* **45**, 583–595.

Jacobsen B., Yin Q.-Z., Moynier F., Amelin Y., Krot A. N., Nagashima K., Hutcheon I. D. and Palme H. (2008) ^{26}Al–^{26}Mg and ^{207}Pb–^{206}Pb systematics of Allende CAIs: canonical solar initial ^{26}Al/^{27}Al ratio reinstated. *Earth Planet. Sci. Lett.* **272**, 353–364.

Kita N. T., Nagahara H., Togashi S. and Morishita Y. (2000) A short duration of chondrule formation in the solar nebula: evidence from ^{26}Al in Semarkona ferromagnesian chondrules. *Geochim. Cosmochim. Acta* **64**, 3913–3922.

Kita N. T., Ushikubo T., Fu B. and Valley J. W. (2009a) High precision SIMS oxygen isotope analysis and the effect of sample topography. *Chem. Geol.* **264**, 43–57.

Kita N., Fournelle J., Mendybaev R., Knight K., Davis A. M., Richter F. M. and Ushikubo T. (2009b) Evaluation of anorthite glass standards for high precision SIMS Al–Mg dating of early solar system materials. *Eos Trans. AGU 90 Fall Meet. Suppl.*, V31E–2020 (abstr.).

Knight K. B., Kita N. T., Davis A. M., Richter F. M. and Mendybaev R. A. (2009) Mg and Si isotope fractionation within three Type B Ca–Al-rich inclusions. *Lunar Planet. Sci.* **40**, #2360.

Kurahashi E., Kita N. T., Nagahara H. and Morishita Y. (2008) ^{26}Al–^{26}Mg systematics of chondrules in a primitive CO chondrite. *Geochim. Cosmochim. Acta* **72**, 3865–3882.

Larsen K. K., Trinquier A., Paton C., Schiller M., Wielandt D., Ivanova M. A., Connelly J. N., Nordlund Å., Krot A. N. and Bizzarro M. (2011) Evidence for magnesium isotope heterogeneity in the solar protoplanetary disk. *Astrophys. J.* **735**, L37.

LaTourrette T. and Hutcheon I. D. (1999) Mg diffusion in melilite: thermal histories for CAIs and their parent bodies. *Lunar Planet. Sci.* **30**, #2003.

LaTourrette T. and Wasserburg G. J. (1998) Mg diffusion in anorthite: implications for the formation of early solar system planetesimals. *Earth Planet. Sci. Lett.* **158**, 91–108.

Lee T., Papanastassiou D. A. and Wasserburg G. J. (1977) Aluminum-26 in the early solar system – fossil or fuel. *Astrophys. J.* **211**, L107–L110.

Liermann H. P. and Ganguly J. (2002) Diffusion kinetics of Fe^{2+} and Mg in aluminous spinel: experimental determination and applications. *Geochim. Cosmochim. Acta* **66**, 2903–2913.

Ludwig K. R. (2003) Isoplot 3.00 A geochronological toolkit for Microsoft Excel. *Berkeley Geochronology Center Special Publication No. 4*, 1–72.

MacPherson G. J. (2007) Calcium–, aluminum-rich inclusions. In *Meteorites, Planets, and Comets* (ed. A. M. Davis), vol. 1. In *Treatise on Geochemistry* (eds. H. D. Holland and K. K. Turekian), second ed. Elsevier, Oxford, Available from:

<http://www.sciencedirect.com/science/referenceworks/9780080437514>.

MacPherson G. J., Paque J. M., Stolper E. and Grossman L. (1984) The origin and significance of reverse zoning in melilite from Allende Type B inclusions. *J. Geol.* **92**, 289–305.

MacPherson G. J., Davis A. M. and Zinner E. K. (1995) The distribution of aluminum-26 in the early solar system: a reappraisal. *Meteoritics* **30**, 365–386.

MacPherson G. J., Simon S. B., Davis A. M., Grossman L., and Krot A. N. (2005) Calcium–aluminum-rich inclusions: major unanswered questions. In *Chondrites and the Protoplanetary Disk* (eds. A.N. Krot, E. R. D. Scott and B. Reipurth), ASP Conference Series, 341, pp. 225–250. Astronomical Society of the Pacific, San Francisco.

MacPherson G. J., Bullock E. S., Janney P. E., Kita N. T., Ushikubo T., Davis A. M., Wadhwa M. and Krot A. N. (2010) Early solar nebula condensates with canonical, not supracanonical, initial $^{26}Al/^{27}Al$ ratios. *Astrophys. J.* **711**, L117–L121.

MacPherson G. J., Kita N. T., Ushikubo T., Bullock E. S. and Davis A. M. (2012) Well-resolved variations in the formation ages for Ca–Al-rich inclusions in the early Solar System. Earth Planet. Sci. Lett. in press. doi:10.1016/j.epsl.2012.03.010.

Makide K., Nagashima K., Krot A. N., Huss G. R., Hutcheon I. D. and Bischoff A. (2009) Oxygen– and magnesium–isotope compositions of calcium–aluminum-rich inclusions from CR2 carbonaceous chondrites. *Geochim. Cosmochim. Acta* **73**, 5018–5050.

McKeegan K. D. et al. (2006) Isotopic compositions of cometary matter returned by Stardust. *Science* **314**, 1724–1728.

McKeegan K. D., Kallio A. P. A., Heber V. S., Jarzebinski G. J., Mao P. H., Coath C. D., Kunihiro T., Wiens R. C., Nordholt J. E., Moses, Jr., R. W., Reisenfeld D. B., Jurewicz A. J. G. and Burnett D. S. (2011) The oxygen isotopic composition of the Sun inferred from captured Solar Wind. *Science* **332**, 1528–1532.

Mendybaev R. A., Richter F. M. and Davis A. M. (2006) Crystallization of melilite from CMAS-liquids and formation of the melilite mantle of Type B1 CAIs: experimental simulations. *Geochim. Cosmochim. Acta* **70**, 2622–2642.

Morioka M. and Nagasawa H. (1991) Diffusion in single crystals of melilite: II. Cations. *Geochim. Cosmochim. Acta* **55**, 751–759.

Nakamura T., Tomeoka K. and Takeda H. (1992) Shock effects of the Leoville CV carbonaceous chondrite – a transmission electron microscope study. *Earth Planet. Sci. Lett.* **114**, 159–170.

Norris T. L., Gancarz A. J., Rokop D. J. and Thomas K. W. (1983) Half-life of ^{26}Al. *Proc. 14th Lunar Planet. Sci. Conf. J. Geophys. Res.* **88**, B331–B333.

Podosek F. A., Zinner E. K., MacPherson G. J., Lundberg L. L., Brannon J. C. and Fahey A. J. (1991) Correlated study of initial $^{87}Sr/^{86}Sr$ and Al–Mg systematics and petrologic properties in a suite of refractory inclusions from the Allende meteorite. *Geochim. Cosmochim. Acta* **55**, 1083–1110.

Richter F. M., Janney P. E., Mendybaev R. A., Davis A. M. and Wadhwa M. (2007a) Elemental and isotopic fractionation of Type B CAI-like liquids by evaporation. *Geochim. Cosmochim. Acta* **71**, 5544–5564.

Richter F. M., Kita N. T., Mendybaev R. A., Davis A. M. and Valley J. W. (2007b) High-precision Mg isotopic composition of Type B1 and B2 CAI melilite. *Lunar Planet. Sci.* **38**, #2303.

Shu F. H., Shang H. and Lee T. (1996) Toward an astrophysical theory of chondrites. *Science* **277**, 1475–1479.

Simon J. I. and Young E. D. (2011) Resetting, errorchrons and the meaning of canonical CAI initial $^{26}Al/^{27}Al$ values. *Earth Planet. Sci. Lett.* **304**, 468–482.

Simon S. B., Joswiak D. J., Ishii H. A., Bradley J. P., Chi M., Grossman L., Aléon J., Brownlee D. E., Fallon S., Hutcheon I. D., Matrajt G. and McKeegan K. D. (2008) A refractory inclusion returned by Stardust from comet 81P/Wild 2. *Meteorit. Planet. Sci.* **43**, 1861–1877.

Stolper E. and Paque J. M. (1986) Crystallization sequences of Ca–Al-rich inclusions from Allende: the effects of cooling rate and maximum temperature. *Geochim. Cosmochim. Acta* **50**, 1785–1806.

Taylor D. J., Cosarinsky M., Liu M.-C., McKeegan K. D., Krot A. N. and Hutcheon I. D. (2005) Survey of initial ^{26}Al in Type A and B CAIs: evidence for an extended formation period for refractory inclusions. *Meteorit. Planet. Sci. Suppl.* **40**, A151.

Thrane K., Bizzarro M. and Baker J. A. (2006) Extremely brief formation interval for refractory inclusions and uniform distribution of ^{26}Al in the early solar system. *Astrophys. J.* **646**, L159–L162.

Valley J. W. and Kita N. (2009) In situ oxygen isotope geochemistry by ion microprobe. Mineralogical Association of Canada Short Course 41, Toronto, May 2009. pp. 19–63.

Wasserburg G. J., Lee T. and Papanastassiou D. A. (1977) Correlated O and Mg isotopic anomalies in Allende inclusions. II – Magnesium. *Geophys. Res. Lett.* **4**, 299–302.

Young E. D., Galy A. and Nagahara H. (2002) Kinetic and equilibrium mass-dependent isotope fractionation laws in nature and their geochemical and cosmochemical significance. *Geochim. Cosmochim. Acta* **66**, 1095–1104.

Young E. D., Simon J. I., Galy A., Russell S. S., Tonui E. and Lovera O. (2005) Supra-canonical $^{26}Al/^{27}Al$ and the residence time of CAIs in the solar protoplanetary disk. *Science* **308**, 223–227.

Yurimoto H., Koike O., Nagahara H., Morioka M. and Nagasawa H. (2000) Heterogeneous distribution of Mg isotopes in anorthite single crystal from Type-B CAIs in Allende meteorite. *Lunar Planet. Sci.* **31**, #1593.

Zolensky M. E. et al. (2006) Mineralogy and petrography of Comet 81P/Wild 2 nucleus sample. *Science* **314**, 1735–1739.

Associate editor: Sara S. Russell